

## Article

# Petrogenesis of Early Cretaceous Granitoids in the Qingdao Area, Jiaodong Peninsula: Constraints from Zircon U–Pb Ages, Geochemistry and Sr–Nd–Hf Isotopes

Yi Ding <sup>1</sup>, Xuejiao Bu <sup>1,\*</sup>, Hong Zhao <sup>2,3,\*</sup>, Shihua Zhong <sup>1</sup>  and Ming Liu <sup>1</sup>

<sup>1</sup> Key Lab of Submarine Geosciences and Prospecting Techniques, MOE and College of Marine Geosciences, Ocean University of China, Qingdao 266100, China; dingyi970624@163.com (Y.D.); zhongshihua@ouc.edu.cn (S.Z.); lm2006happy@ouc.edu.cn (M.L.)

<sup>2</sup> Key Laboratory of Rhenium-Osmium Isotopic Geochemistry, National Research Center for Geoanalysis CAGS, Beijing 100037, China

<sup>3</sup> Institute of Geological Survey, China University of Geosciences, Wuhan 430074, China

\* Correspondence: 2004bxj@ouc.edu.cn (X.B.); zhaohong@mail.cgs.gov.cn (H.Z.)

**Abstract:** The Jiaodong Peninsula is located on the junction of the North China Craton (NCC) and South China Block (SCB), where Mesozoic igneous rocks are widespread. However, the petrogenesis and tectonic settings for these Mesozoic igneous rocks are still controversial. In this study, we present detailed geochronological and geochemical analyses of quartz monzonite, monzogranite, syenogranite, and alkali feldspar granite in the Qingdao area, east of the Jiaodong Peninsula, to constrain their petrogenesis and tectonic setting. Zircon U–Pb dating shows that they mainly formed in the Early Cretaceous (120.5–113.1 Ma). Quartz monzonite exhibits adakitic geochemical features (e.g., low Y and high Sr/Y). Combined with its Sr–Nd–Hf isotopic features, we suggest that quartz monzonite may have been produced by the partial melting of phengite-bearing eclogites at the base of the thickened continental crust of the NCC. In contrast, monzogranite and syenogranite exhibit I-type granite affinities, whereas alkali feldspar granite exhibits features consistent with A-type granite. The strongly negative  $\varepsilon_{\text{Hf}}(t)$  and  $\varepsilon_{\text{Nd}}(t)$  values of the I-type rocks indicate that they were most likely produced through partial melting of granitic gneisses from the NCC, whereas A-type magmas may be formed through fractional crystallization from the non-adakitic granitic magma. Combined with previous studies, we suggest that these granitoids were formed in a lithospheric extensional setting via the rollback of the subducted Paleo-Pacific slab, which resulted in the reworking of the deep crust beneath the Sulu ultrahigh-pressure metamorphic belt.

**Keywords:** zircon dating; adakite; A-type granite; I-type granite; North China Craton



**Citation:** Ding, Y.; Bu, X.; Zhao, H.; Zhong, S.; Liu, M. Petrogenesis of Early Cretaceous Granitoids in the Qingdao Area, Jiaodong Peninsula: Constraints from Zircon U–Pb Ages, Geochemistry and Sr–Nd–Hf Isotopes. *Minerals* **2023**, *13*, 963. <https://doi.org/10.3390/min13070963>

Academic Editor: Aleksei V. Travin

Received: 31 May 2023

Revised: 6 July 2023

Accepted: 14 July 2023

Published: 20 July 2023



**Copyright:** © 2023 by the authors. Licensee MDPI, Basel, Switzerland. This article is an open access article distributed under the terms and conditions of the Creative Commons Attribution (CC BY) license (<https://creativecommons.org/licenses/by/4.0/>).

## 1. Introduction

The Sulu orogenic belt is formed by collision between the North China Craton (NCC) and South China Block (SCB) during the Triassic [1–3]. Despite several decades of studies from geophysics, petrology, and geochemistry regarding the crustal architecture and components beneath the Sulu belt, many aspects about this orogenic belt are still in hot debate [4–7]. One of controversies lies on petrogenesis, magma sources, and tectonic settings of granitoids occurring in this area, which in turn hinder a better understanding regarding the tectonic evolution of NCC and Sulu belt [8–10].

The Qingdao granitoids from large-scale plutons in the Sulu belt can be subdivided into several rock types [11]. Previous studies show that the granitoids in the Qingdao and adjacent areas were mainly formed in the Early Cretaceous, which is consistent with the major magmatic events in the eastern NCC [11–13]. The granitoids are suggested to be derived from partial melting of the subducted continental crust, according to their enriched light rare-earth elements (LREEs) and depleted high-field-strength elements (HFSE), as

well as high  $(^{87}\text{Sr}/^{86}\text{Sr})_I$  ratios and low  $\epsilon_{\text{Nd}}(t)$  [14,15]. However, some granitoids exhibit geochemical properties that are consistent with the contemporaneous mafic rock veins in the study area [16], which might indicate that granitoids could be probably related to the interaction of subducted crust and mantle-derived magma [17]. To address these questions, in this study we conducted a detailed investigation on the granitoids occurring in the Qingdao area, combined with zircon U–Pb age, whole-rock major, trace elements, Sr–Nd isotopes, and zircon Lu–Hf isotopes. Our aim is to reveal their petrogeneses and tectonic backgrounds, which in turn help to better understand the tectonic evolution of the Sulu orogenic belt.

## 2. Geological Setting and Petrography

The Sulu orogenic belt, also called Sulu ultrahigh-pressure metamorphic belt, was formed by a collision between the North China Craton (NCC) and South China Block (SCB) during the Triassic [2,18]. Three secondary tectonic units—the Jiaobei uplift, the Jiaolai fault depression, and the Jiaonan–Weihai exhumation zone—were formed due to the westward subduction of the Pacific plate. The Qingdao area is in the southeast of the Jiaodong Peninsula, and a special structural zone at the junction of the eastern end of the Jiaonan–Weihai exhumation zone and the Jiaolai fault depression (Figure 1).

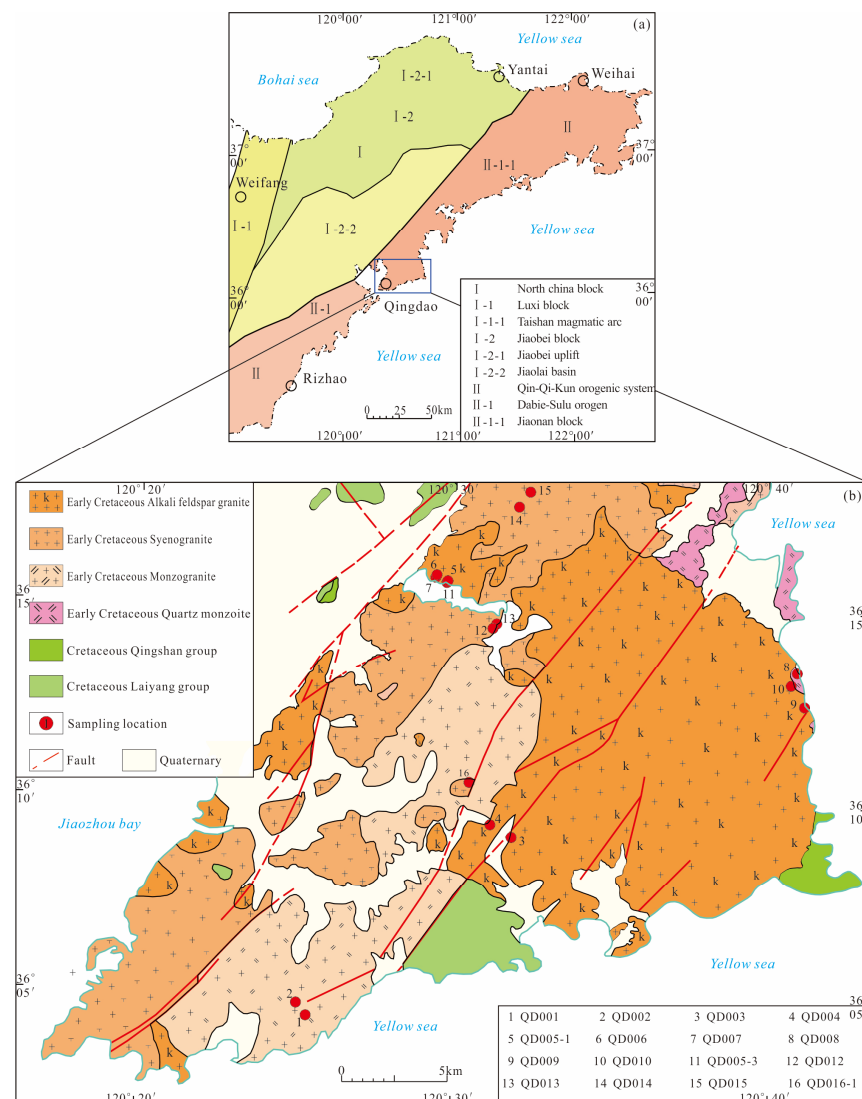


**Figure 1.** (a) Tectonic framework of the Jiaodong Peninsula. (b) Geological map and sampling location of the Qingdao granitoids.

Late Mesozoic granitoid plutons are widely distributed in the Qingdao area, which was a part of the Mesozoic granitoid belt in eastern China. These granitoid plutons intruded the Cretaceous volcanic, Jurassic–Cretaceous sedimentary, and Precambrian metamorphic rocks of the Jiaonan Group. Twenty-one granitoid samples, ranging from fine- to coarse-grained and greatly variable in texture, were collected for this study. The granitoids can be divided into two types according to their quartz content: (1) quartz monzonite, consisting of plagioclase (35%–40%), K-feldspar (25%–30%), quartz (5%–10%), hornblende (15%–20%), biotite (5%), and accessory minerals including magnetite, titanite, zircon and (2) granites, composed of plagioclase (5%–35%), K-feldspar (30%–65%), quartz (20%–30%), biotite (5%–10%), and accessory minerals including magnetite, titanite, apatite, and zircon. Based on the petrographic characteristics, the granites can be further divided into three types: monzogranite, syenogranite, and alkali feldspar granite. The locations of the twenty-one samples are shown in Figure 1 and detailed geological information can be found in Table 1 and Figure 2.

**Table 1.** Petrographic characteristics and age of the studied granitoids in the Qingdao area.

Sample No.	Lithology	Main Mineral Component	U-Pb Age (Ma)
QD001-3	Monzogranite porphyry	K-feldspar (35%), plagioclase (30%), quartz (25%), biotite (5%)	119.2 ± 1.4
QD001-4	Monzogranite	K-feldspar (40%), plagioclase (30%), quartz (20%), biotite (5%)	-
QD002-2	Monzogranite	K-feldspar (35%), plagioclase (25%), quartz (25%), biotite (10%)	120.2 ± 1.3
QD002-4	Monzogranite porphyry	K-feldspar (30%), plagioclase (25%), quartz (30%), biotite (5%)	-
QD003-1	Alkali feldspar granite	K-feldspar (60%), plagioclase (5%), quartz (20%), biotite (10%)	118.6 ± 1.4
QD003-5	Alkali feldspar granite	K-feldspar (65%), plagioclase (5%), quartz (20%), biotite (5%)	-
QD004-3	Alkali feldspar granite	K-feldspar (60%), plagioclase (5%), quartz (25%), biotite (5%)	-
QD005-1	Alkali feldspar granite	K-feldspar (60%), plagioclase (10%), quartz (20%), biotite (5%)	113.1 ± 1.6
QD006-1	Alkali feldspar granite	K-feldspar (65%), plagioclase (5%), quartz (20%), biotite (5%)	-
QD007-1	Alkali feldspar granite	K-feldspar (60%), plagioclase (5%), quartz (25%), biotite (5%)	-
QD008-1	Monzogranite	K-feldspar (25%), plagioclase (40%), quartz (10%), hornblende (15%), biotite (5%)	120.5 ± 1.2
QD009-1	Alkali feldspar granite	K-feldspar (65%), plagioclase (5%), quartz (20%), biotite (5%)	117.0 ± 1.1
QD010-2	Alkali feldspar granite	K-feldspar (60%), plagioclase (10%), quartz (20%), biotite (5%)	-
QD012-1	Syenogranite	K-feldspar (40%), plagioclase (20%), quartz (25%), biotite (10%)	117.4 ± 1.4
QD013-1	Syenogranite	K-feldspar (45%), plagioclase (15%), quartz (25%), biotite (10%)	-
QD014-1	Syenogranite	K-feldspar (45%), plagioclase (20%), quartz (20%), biotite (10%)	-
QD015-1	Alkali feldspar granite	K-feldspar (65%), plagioclase (5%), quartz (20%), biotite (5%)	117.7 ± 1.2
QD016-1	Syenogranite	K-feldspar (45%), plagioclase (20%), quartz (25%), biotite (5%)	119.4 ± 1.3

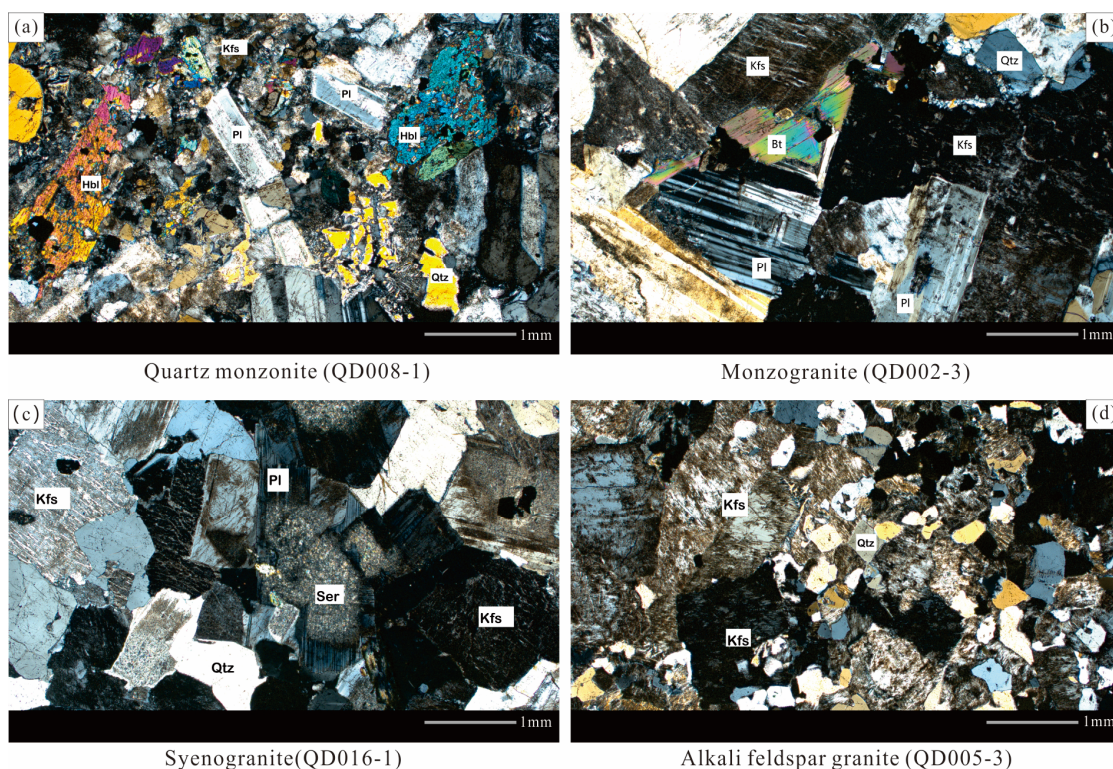


**Figure 2.** Photomicrographs showing minerals and textures of the granitoids in the Qingdao area. (a) Quartz monzonite (sample QD008-1). (b) Monzogranite (sample QD002-3). (c) Syenogranite (sample QD016-1). (d) Alkali feldspar granite (sample QD005-3). Abbreviations: Qtz—quartz; Kfs—K-feldspar; Pl—plagioclase; Ser—sericite; Bt—biotite.

### 3. Methods

#### 3.1. Zircon U–Pb Dating and Zircon Lu–Hf Isotopes

Separation of zircon was performed in the Laboratory of the Langfang Institute of Regional Geological Survey by standard crushing, sieving, heavy liquid, and magnetic separation techniques. The selected zircons were mounted in an epoxy block before being polished to obtain an even surface. Cathodoluminescence (CL) images were taken on a JSM-IT100 scanning electron microscope at Wuhan Sample Solution Analytical Technology Co., Ltd. to identify the internal structure and texture of zircon grains.

Zircon U–Pb dating was carried out using an Agilent 7900 inductively coupled plasma mass spectrometer (ICP-MS) equipped with a 193 nm laser ablation system in the Ocean Lithosphere and Mantle Dynamics Laboratory, Institute of Oceanology, Chinese Academy of Sciences (OLMDL, IO, CAS). Helium was applied as a carrier gas, whereas the spot size of the laser was set to 35 or 25  $\mu\text{m}$  in this study. Zircon 91,500 and glass NIST610 were used as reference materials for U–Pb dating and trace element calibration, respectively. An Excel-based software, ICPMSDataCal, was used to perform off-line selection and integration of background and analyzed signals, time-drift correction, and quantitative calibration for trace element analysis and U–Pb dating. Concordia diagrams and weighted mean calculations were made using the IsoplotR software of Vermeesch [19].

Zircon Lu–Hf isotope compositions were analyzed using a multicollector inductively coupled plasma mass spectrometer (MC-ICP-MS) coupled with an excimer laser ablation (LA) system at the Tianjin Institute of Geology and Mineral Resources. All the points selected for zircon Lu–Hf isotope analysis were in situ or around the U–Pb dating points.

#### 3.2. Major and Trace Elements

The whole-rock major elements were analyzed using an Axios PW4400 X-ray fluorescence spectrometer (Malvern Panalytical, Malvern, UK) at the Tianjin Institute of Geology

and Mineral Resources. The test conditions were voltage 50 kV and current 60 mA. Analyses of USGS rock reference materials (GBW07101-14, BCR-2, and BHVO-1) indicate a precision and accuracy of better than 5%. Whole-rock trace element analyses were conducted with an Agilent 7900e ICP-MS (Santa Clara, CA, USA) at OLMDL, IO, CAS. The analytical precision was better than 5% for most trace elements.

### 3.3. Sr–Nd Isotopes

Sr–Nd isotope analyses were performed by a Neptune Plus MC-ICP-MS (Thermo Fisher Scientific, Dreieich, Germany) at the Wuhan Sample Solution Analytical Technology Co., Ltd., Wuhan, China. The USGS reference materials BCR-2 (basalt) and RGM-2 (rhyolite) were used as reference materials for Sr–Nd isotope dating calibration. The  $^{87}\text{Sr}/^{86}\text{Sr}$  analysis values of RGM-2 and BCR-2 are  $0.704173 \pm 20$  and  $0.705012 \pm 20$ , respectively. The  $^{143}\text{Nd}/^{144}\text{Nd}$  test values of RGM-2 and BCR-2 are  $0.512641 \pm 11$  and  $0.512804 \pm 12$ , respectively.

## 4. Results

### 4.1. Zircon U–Pb Ages and Lu–Hf Isotopes

In this study, nine samples were used for zircon U–Pb dating and Lu–Hf isotopic analyses. The CL images of quartz monzonite and granite show that most zircons are euhedral to subhedral (Figure 3) with typical magmatic oscillatory zoning ( $\text{Th}/\text{U} > 0.1$ ). These features collectively indicate that they are of magmatic origin. The quartz monzonite yielded a weighted mean  $^{206}\text{Pb}/^{238}\text{U}$  age of  $120.5 \pm 1.2$  Ma (sample QD008-1). The monzogranite yielded weighted mean  $^{206}\text{Pb}/^{238}\text{U}$  ages of  $119.2 \pm 1.4$  Ma (sample QD001-3) and  $120.2 \pm 1.3$  Ma (sample QD002-2), respectively. The syenogranite yielded weighted mean  $^{206}\text{Pb}/^{238}\text{U}$  ages of  $117.4 \pm 1.4$  (sample QD0012-1) and  $119.4 \pm 1.3$  (sample QD0016-1), respectively. The alkali feldspar granite yielded weighted mean  $^{206}\text{Pb}/^{238}\text{U}$  ages of  $118.6 \pm 1.4$  (sample QD003-1),  $113.1 \pm 1.6$  Ma (sample QD005-1),  $117.0 \pm 1.1$  Ma (sample QD009-1), and  $117.7 \pm 1.2$  Ma (sample QD0015-1), respectively. These results indicate that the crystallization age of the granitoids from the Qingdao area was in the Early Cretaceous (Table S1, Figure 4).

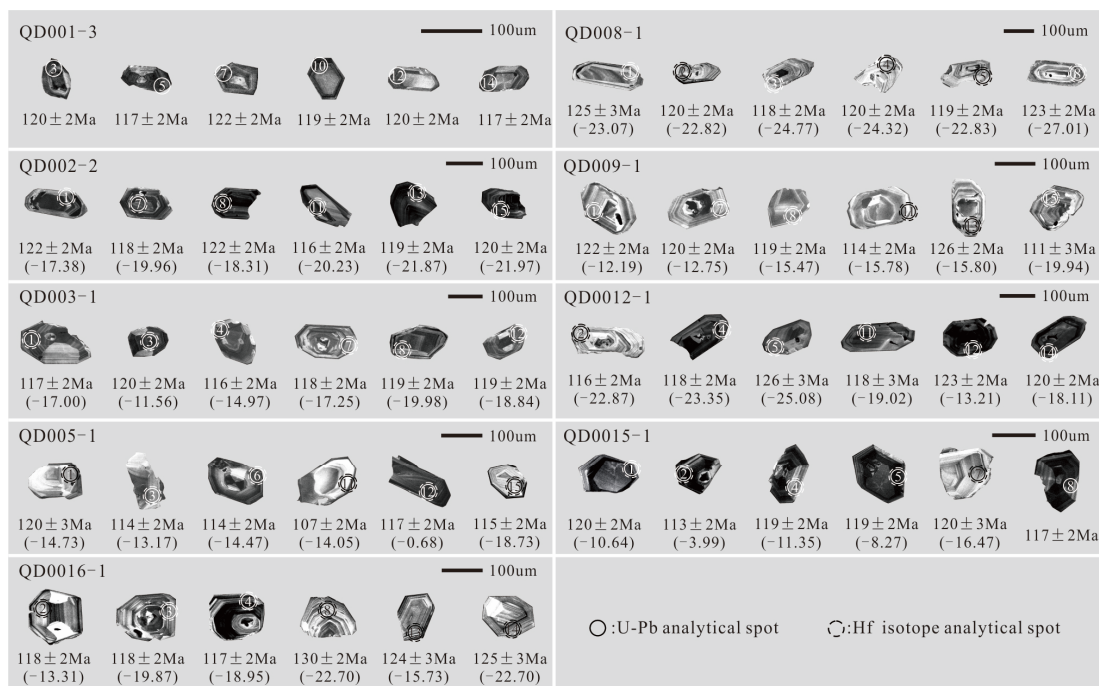


**Figure 3.** CL images of typical zircons from the Qingdao granitoids. The numbers adjacent to circles refer to the zircon  $^{206}\text{Pb}/^{238}\text{U}$  ages (Ma) and  $\epsilon_{\text{Hf}}(t)$  values.

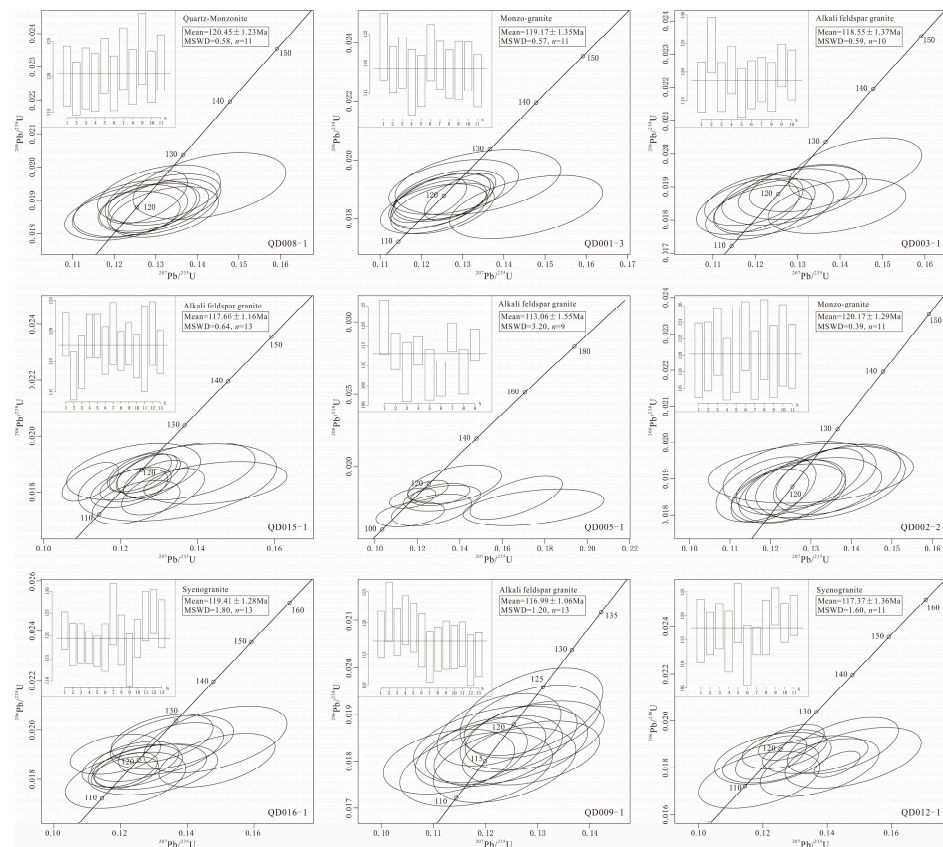


**Figure 4.** Concordia diagram of zircon U–Pb dating results for the Qingdao granitoids. The ages in the diagram refer to the weighted mean  $^{206}\text{Pb}/^{238}\text{U}$  ages (Ma).

The zircon  $\varepsilon_{\text{Hf}}(t)$  values for alkali feldspar granite are between  $-0.68$  and  $-25.08$ , with the corresponding two-stage model ages ranging from 1213 to 2437 Ma. The  $\varepsilon_{\text{Hf}}(t)$  values of the other granites are relatively low, and the two-stage model ages range from 2009 to 2755 Ma. The quartz monzonite samples show  $\varepsilon_{\text{Hf}}(t)$  values ranging from  $-22.82$  to  $-27.01$ , and the two-stage model age ranging from 2614 to 2876 Ma (Table S2).

#### 4.2. Whole-Rock Element Geochemistry

The major and trace element data are summarized in Table S3. The granitoids have variable  $\text{K}_2\text{O}$  contents, which fall in the high-K calc-alkaline and shoshonitic fields on the  $\text{K}_2\text{O}$  vs.  $\text{SiO}_2$  diagram (Figure 5). Almost all the samples are subalkaline on the total alkalis versus silica (TAS) diagram (Figure 6a). There are two categories of granitoids in this paper based on the  $\text{SiO}_2$  content, which are consistent with the micrograph observations: (1) quartz monzonite with  $\text{SiO}_2$  less than 70%, which falls in the domain of quartz monzonite in the TAS diagram (Figure 6a); (2) the granites include monzogranite, syenogranite, and alkali feldspar granite with varying  $\text{SiO}_2$  contents of more than 70%. The quartz monzonite samples are metaluminous (Figure 6b), with  $A/\text{CNK}$  ( $\text{Al}_2\text{O}_3/\text{CaO} + \text{Na}_2\text{O} + \text{K}_2\text{O}$ ) of 0.82–0.83, and high in  $\text{K}_2\text{O}$  (3.93%–3.96%),  $\text{Al}_2\text{O}_3$  (15.45%–15.56%), Sr (>400 ppm), and Ba (1468–1646 ppm) concentrations and Sr/Y ratios (58.1–58.3); they are low in  $\text{TiO}_2$  (0.55%–0.56%) and Rb (53.08–53.69 ppm) (Table S3, Figure 7). The granites are metaluminous to weakly peraluminous ( $A/\text{CNK} = 0.98$ –1.05, Figure 6b) and are relatively low in CaO (0.07%–1.66%),  $\text{TiO}_2$  (0.12%–0.28%),  $\text{Fe}_2\text{O}_3$  (0.08%–0.43%), MgO (0.04%–0.36%),  $\text{P}_2\text{O}_5$  (0.01%–0.26%), Sr (10.78–166.60 ppm), and Ba (27.14–653.26 ppm) concentrations and Sr/Y ratios but high in Rb (136.65–295.51 ppm) and Rb/Sr ratios (Table S3, Figure 7).

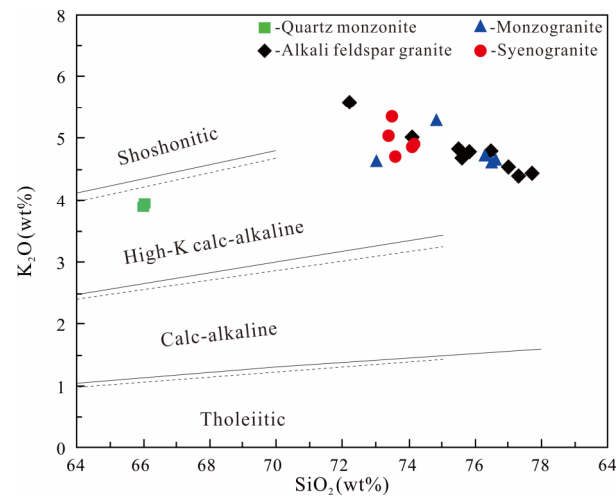


Figure 5.  $K_2O$  vs.  $SiO_2$  diagrams for the Qingdao granitoids (modified after [20]).

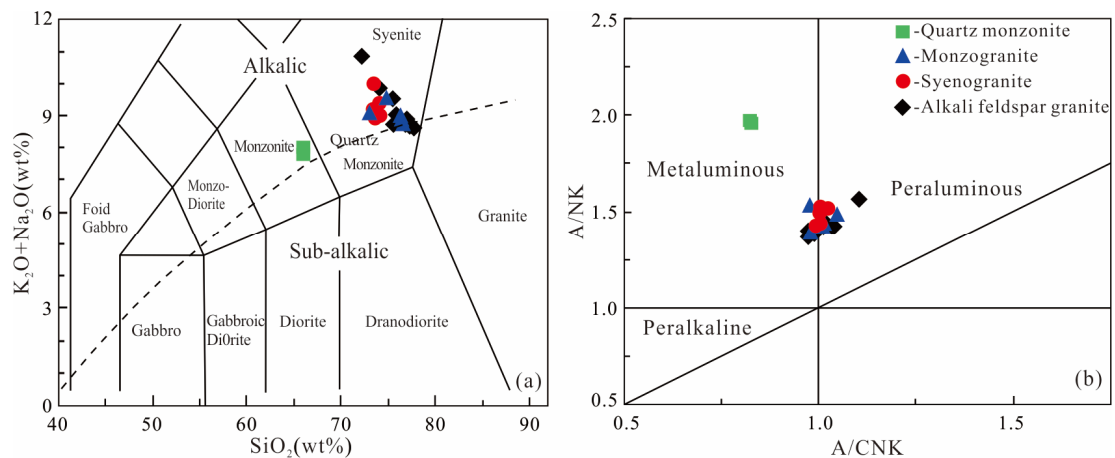
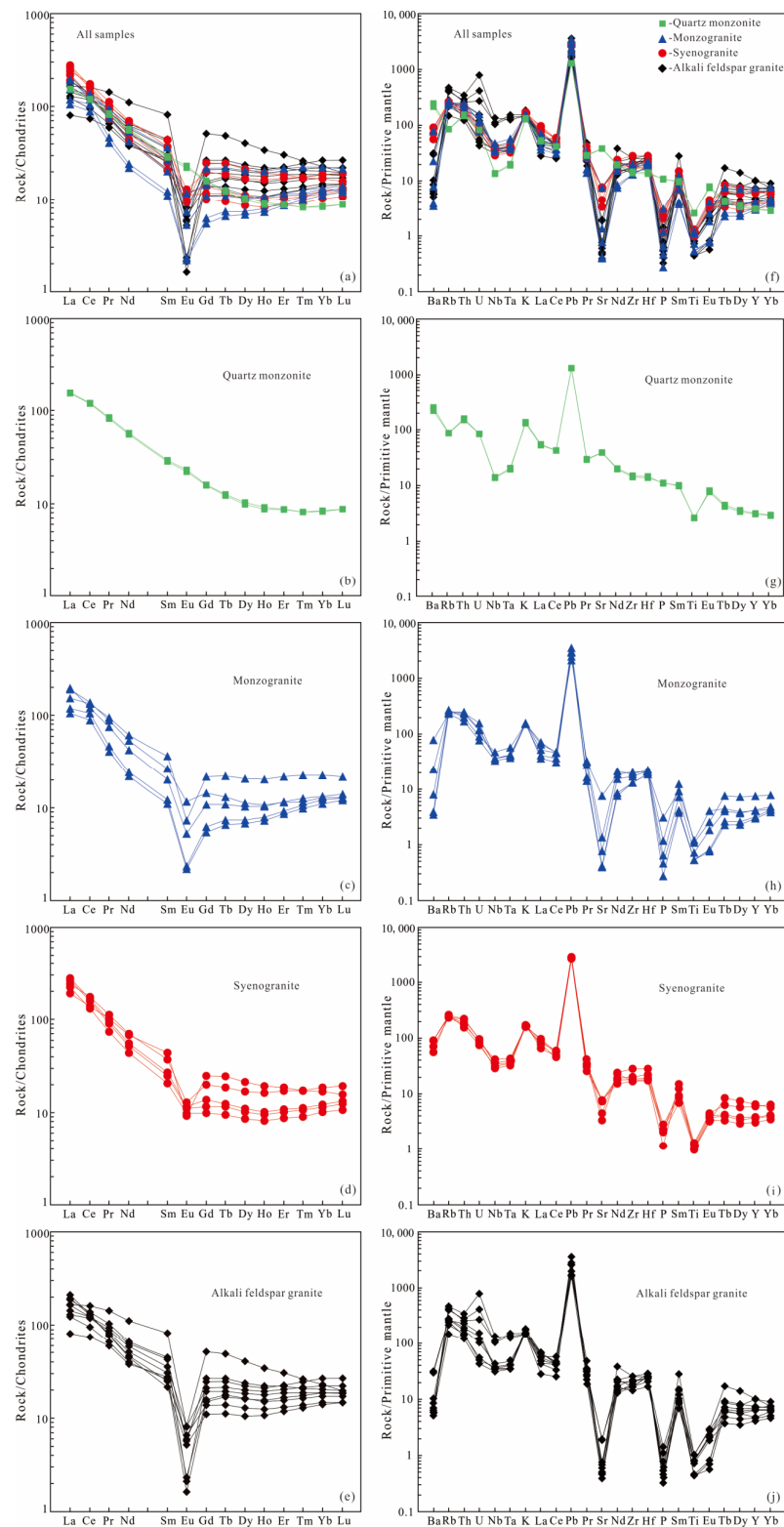


Figure 6. (a) Total alkalis vs. Silica (modified after [21]) and (b)  $A/NK$  vs.  $A/CNK$  (modified after [22]) diagrams.

The Zr saturation temperatures of granitoids are also calculated according to the method given by Boehncke [23] and are shown in Table S3. The saturation temperature values range from 675 °C to 810 °C for the Qingdao granitoids.

#### 4.3. Sr–Nd Isotopes

Whole-rock Sr–Nd isotopic data for the granitoid samples are presented in Table S3. The  $\epsilon_{Nd}(t)$  and  $(^{87}Sr/^{86}Sr)_I$  values are calculated for the ages of magma crystallization. The quartz monzonites have high  $(^{87}Sr/^{86}Sr)_I$  ratios of 0.7088 and negative  $\epsilon_{Nd}(t)$  values of  $-16.7$ . The single-stage model age ( $T_{DM1}$ ) is 1931 Ma, and the two-stage model age ( $T_{DM2}$ ) is 2271 Ma.  $(^{87}Sr/^{86}Sr)_I$  ratios and  $\epsilon_{Nd}(t)$  values of monzogranite (sample QD0016-1) are 0.7079 and  $-17.71$ , respectively, with  $T_{DM1}$  and  $T_{DM2}$  ages being 1928 Ma and 2353 Ma, respectively (Table S3).



**Figure 7.** REE and trace element diagrams for the granitoids in the Qingdao area. (a) Chondrite-normalized REE diagrams for all studied samples. (b–e) Individual chondrite-normalized REE diagrams for quartz monzonite, monzogranite, syenogranite and alkali feldspar granite samples, respectively. (f) Primitive mantle-normalized trace element diagrams for all studied samples. (g–j) Primitive mantle-normalized trace element diagrams for quartz monzonite, monzogranite, syenogranite and alkali feldspar granite samples, respectively. The chondrite REE and primitive mantle normalization values are from [24].

## 5. Discussion

### 5.1. Timing of Emplacement for the Qingdao Granitoids

U–Pb dating data from this study show that the granitoids in the Qingdao area formed in 120.5–113.1 Ma (Early Cretaceous) (Table S1, Figure 4). These ages are similar to the previous studies. For example, SHRIMP zircon U–Pb ages obtained by Zhao et al. range from 110.8 to 146.8 Ma [11]. Gao et al. reported zircon U–Pb ages of 120 Ma for the Laoshan granites [17]. Yan et al. reported a SHRIMP zircon U–Pb age of 115 Ma [15]. Therefore, the Qingdao granitoids formed after approximately 120 Ma in response to the collision of the NCC and SCB [25–30].

### 5.2. The Petrogenesis and Magma Source

#### 5.2.1. Quartz Monzonite

The quartz monzonite samples fall within the I-type or S-type fields (Figure 8), but they are metaluminous with low A/CNK (0.82–0.83) values and do not contain aluminum minerals, e.g., muscovite, garnet, cordierite, or tourmaline, which is an obvious difference from typical strong peraluminous S-type granites. In addition, the trace elemental features of the quartz monzonite are below the minimum for A-type granites [31], having Zr + Nb + Ce + Y contents of 253–263 ppm and lower  $10,000 \times \text{Ga}/\text{Al}$  ratio (1.95–1.98). Then, quartz monzonite is classified as an I-type granitoid.

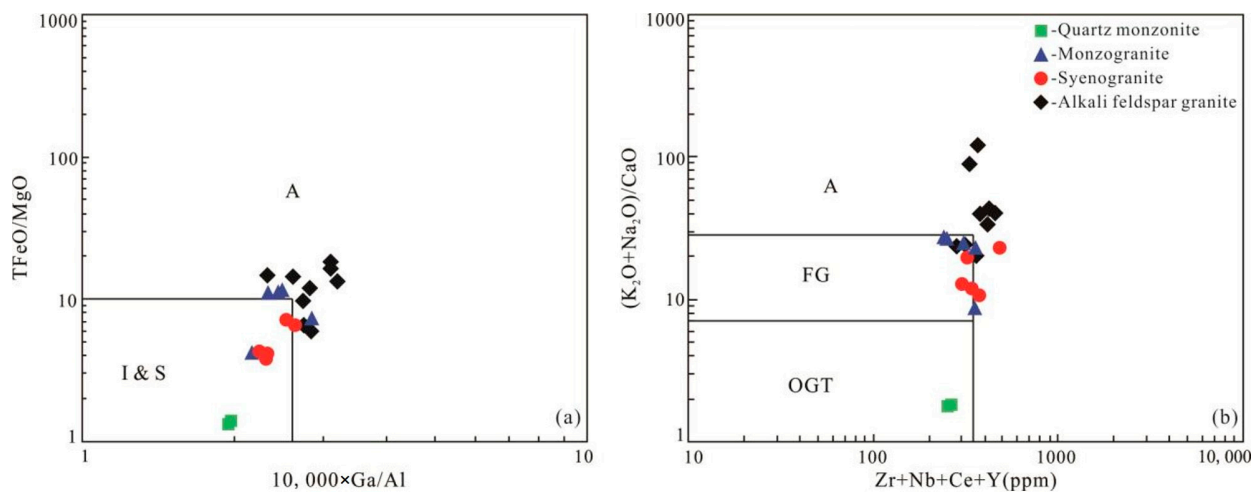


**Figure 8.** Variation diagrams of (a)  $10,000 \times \text{Ga}/\text{Al}$  vs.  $\text{FeO}^{\text{T}}/\text{MgO}$  and (b) Zr + Ce + Nb + Y vs.  $(\text{Na}_2\text{O} + \text{K}_2\text{O})/\text{CaO}$  for the Qingdao granitoids (modified after [31]. FG: Fractionated granites; OGT: Unfractionated I-, S-, and M-type granites).

The quartz monzonite is characterized by high Sr contents but low Yb and Y contents; strongly fractionated REE patterns; and high Sr/Y and  $(\text{La}/\text{Yb})_{\text{N}}$  ratios with negligible or weakly positive Eu anomalies (Figures 5–7), which are geochemical features similar to those of adakite-like granitoids (Figure 9) [32–36]. Generally, there are three common petrogenetic models of adakite-like granitoids: (1) the mixing of mafic magma and felsic magma coupled with fractional crystallization (AFC) [33,36,37]; (2) the melting of the delaminated lower crust with addition of mantle material [38–40]; and (3) the partial melting of the thickened lower crust [29,30,41].

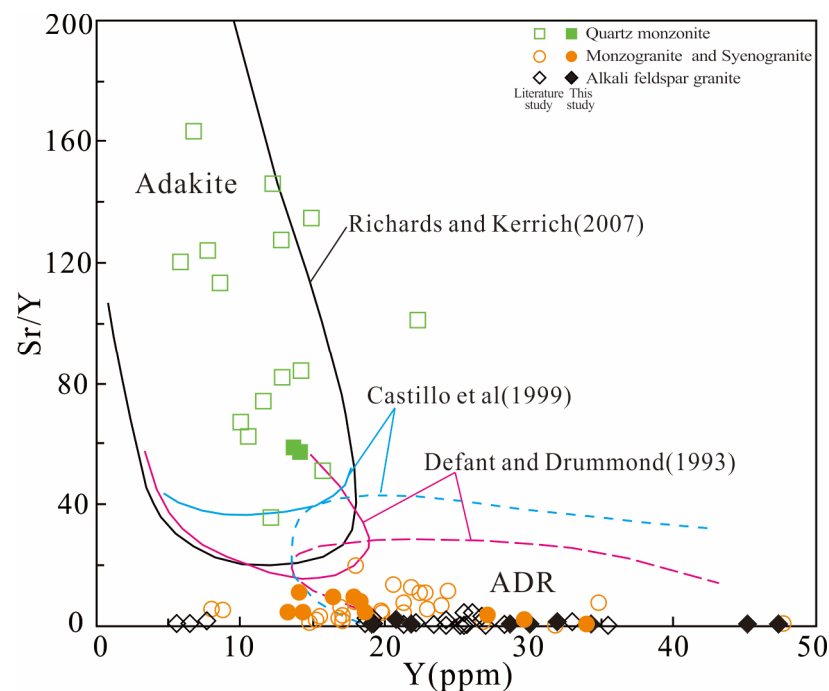


**Figure 9.** Sr/Y vs. Y diagram for the Qingdao granitoids. The literature data sources are from [11,15,17]. The solid line indicates the Adakite range, and the dotted line indicates the ADR range. The black lines are from [35]. The blue lines are from [34], and the orange lines are from [32].

The quartz monzonite generally exhibits high  $\text{SiO}_2$  and  $\text{K}_2\text{O}$ , low Cr and Ni, strong depletion of Nb and Ta, negative  $\epsilon_{\text{Hf}}(t)$  ( $-22.82$  to  $-27.01$ ) and  $\epsilon_{\text{Nd}}(t)$  ( $-16.71$ ) values, and older  $T_{\text{DM2}}$  ages (2.8–2.6 Ga), suggesting that the derivation of adakitic rocks was mainly from the continental crust rather than mantle material. Moreover, there are no large-volume mafic rocks or mafic xenoliths/enclaves in the study area. Then, it is unlikely that the petrogenesis of the quartz monzonite plutons was related to mantle-derived mafic magma [13,42–44]. In addition, if the quartz monzonite was formed by crystallization differentiation of mafic magma, the original magma should have higher Sr contents and Sr/Y and  $(\text{La}/\text{Yb})_{\text{N}}$  values. However, the Early Cretaceous mafic rocks that do occur in the study area have lower Sr/Y and  $(\text{La}/\text{Yb})_{\text{N}}$  values than quartz monzonite [42,45]. Additionally, most trace elements (e.g., Sr, La,  $\text{La}/\text{Yb}$ ) of quartz monzonite are extremely depleted with increasing  $\text{SiO}_2$  (Figure 10). Then, the Quartz monzonite with higher Sr/Y and  $(\text{La}/\text{Yb})_{\text{N}}$  values is unlikely to be formed by the fractional crystallization of mafic magma. Adakite-like rocks derived from melting of delaminated mafic lower crustal rocks generally have extremely high Mg# (normally  $> 40$ ) and Ni ( $\geq 20$  ppm) contents but low  $\text{SiO}_2$  and  $\text{K}_2\text{O}$  contents, attributed to interaction with the peridotitic asthenospheric mantle during the ascent of slab melts [35,36,46]. But the quartz monzonite from Qingdao exhibits relatively lower contents of MgO and Ni than delaminated lower crust. So, the quartz monzonite in the study area was considered to be unlikely to have been derived from the partial melting of delaminated lower crust with the addition of mantle material. Therefore, the studied quartz monzonite may be formed by the partial melting of thickened lower crust.

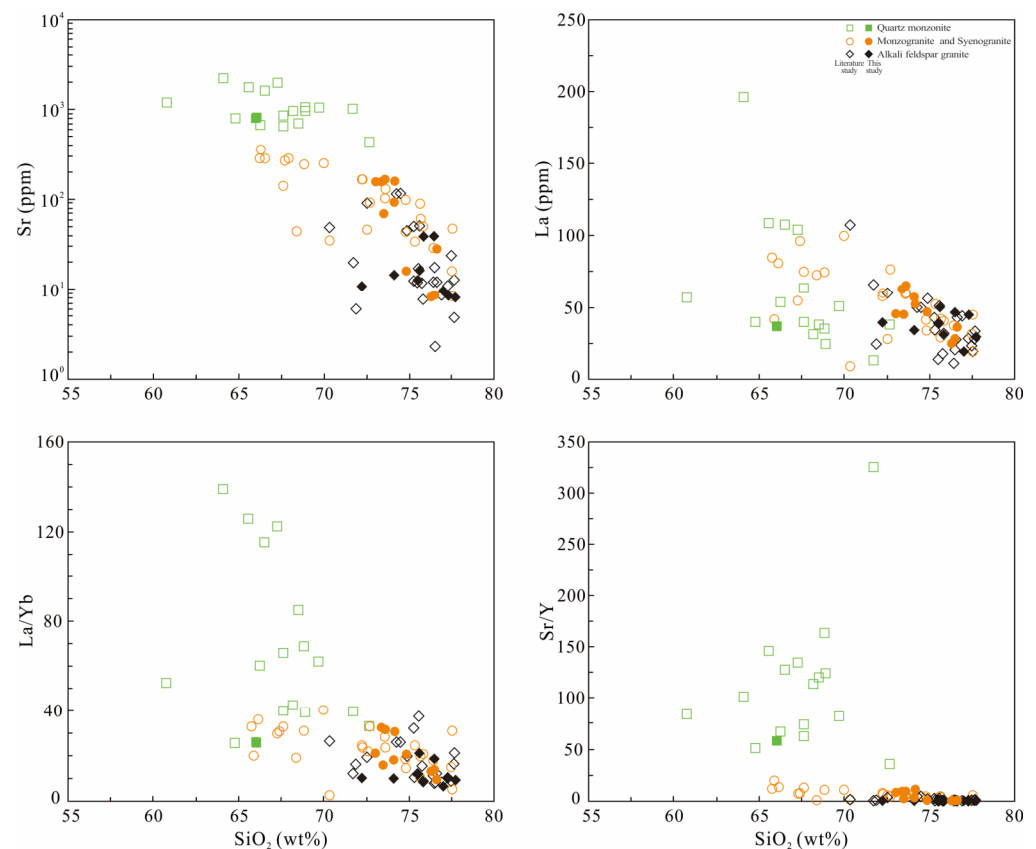


**Figure 10.** Plots of trace elements vs.  $\text{SiO}_2$  for the Qingdao granitoids. The literature data sources are from [11,15,17].

The high LREE, low HREE, and weakly negative Eu anomaly values of the quartz monzonite (Figure 7a) indicate that garnet remains in the magma source as residual material. However, the HREE distribution pattern is flat with  $(\text{Ho}/\text{Yb})_N$  of 1.02–1.05 (Figure 7a), suggesting that amphibole may be the main residual mineral. It means that eclogite or garnet amphibolite may be the residual phase after the partial melting of the mafic lower crust. Experimental petrological studies suggest that a tonalite–trondhjemite melt can be produced by the partial melting of metabasic rocks [47–49]. At a higher temperature and pressure (15–20 kb, 1000 °C), the melt formed by dehydration melting phengite-bearing eclogite is characterized by low Mg and high K contents, high Sr/Y and La/Yb ratios, LREE enrichment and HREE depletion, positive Eu anomaly, and Nb–Ta deficit [50], which are consistent with the geochemical characteristics of quartz monzonite. Moreover, as shown in Figure 11, the Sr–Nd isotopic composition of the quartz monzonite samples fall into the range of the Dabie–Sulu UHP eclogites [43]. In addition, the characteristics of trace elements show negative Nb–Ta anomaly, high  $(^{87}\text{Sr}/^{86}\text{Sr})_I$  ratios (0.708487), low  $\epsilon_{\text{Hf}}(t)$  values (−21.90~−24.87),  $\epsilon_{\text{Nd}}(t)$  values (−16.08~−16.71), and old two-stage model ages ( $T_{\text{DM}2}$ ) (2495~2694 Ma), which are similar to the adakitic rocks derived from the partial melting of thickened lower crust in the Jiaodong Peninsula [30,51]. In conclusion, the quartz monzonite in the Qingdao area could be generated by partial melting eclogite under pressure conditions of 15–20 kb and at the corresponding depth of 50–65 km.

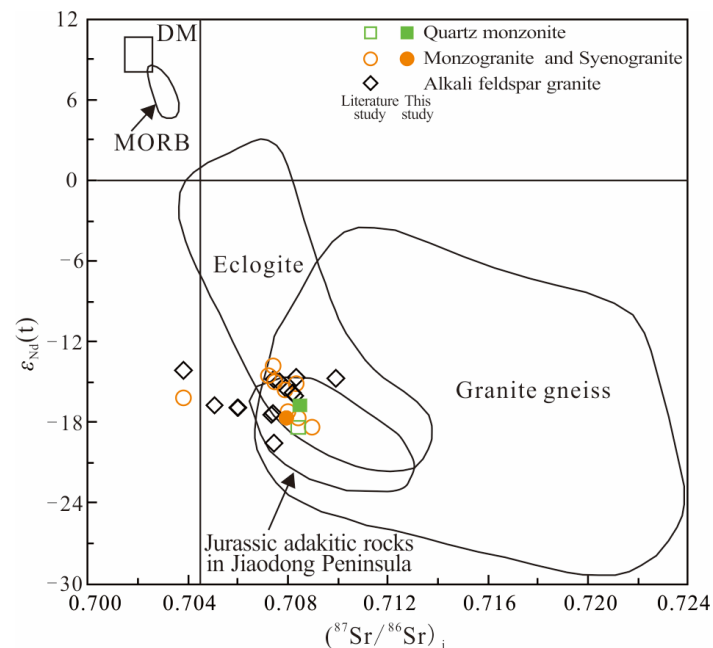


**Figure 11.**  $(^{87}\text{Sr}/^{86}\text{Sr})_i$  vs.  $\epsilon_{\text{Nd}}(t)$  for the Qingdao granitoids (modified after [30]). The ages for quartz monzogranite and monzogranite are 120.5 Ma and 119.4 Ma, respectively, which are used to calculate the  $(^{87}\text{Sr}/^{86}\text{Sr})_i$  and  $\epsilon_{\text{Nd}}(t)$ . The literature data sources are from [11,15,17].

### 5.2.2. Monzogranite and Syenogranite

The monzogranite and syenogranite are characterized by remarkably negative Eu anomalies, low  $\text{FeO}^T/\text{MgO}$ ,  $10,000 \times \text{Ga}/\text{Al}$  ratios and  $\text{Zr} + \text{Nb} + \text{Ce} + \text{Y}$  contents (253–263 ppm), which are below the specified minimums for A-type granites [31]. They are similar to I-type or S-type granites rather than A-type granites. As shown in Figure 8, most samples fall within the I-type or S-type fields. Moreover, they are metaluminous or weakly peraluminous with low  $A/\text{CNK}$  values (0.74–1.05) and do not contain aluminum minerals, e.g., muscovite, garnet, cordierite, or tourmaline, which are obvious differences from typical strong peraluminous S-type granite. In addition, the  $\text{SiO}_2$  vs.  $\text{P}_2\text{O}_5$  (Figure 12) contents show a strong negative correlation, indicating that they are similar to the trend of I-type granitoids, but not S-type granitoids.

The depletion in Ba, Sr, P, Ti, Nb, and Ta of monzogranite and syenogranite indicated that the rocks experienced a high crystallization differentiation after partial melting. The negative anomalies of Sr and Ba are mainly caused by the crystallization differentiation of alkali feldspar. As shown in the Sr vs. Ba plot (Figure 13), alkali feldspar is a major fractionation phase, which can also interpret the Ba depletion, while the low Sr/Y ratios (0.61–11.27) and significant negative Eu anomalies are considered to be connected with the fractionation of plagioclase [52].

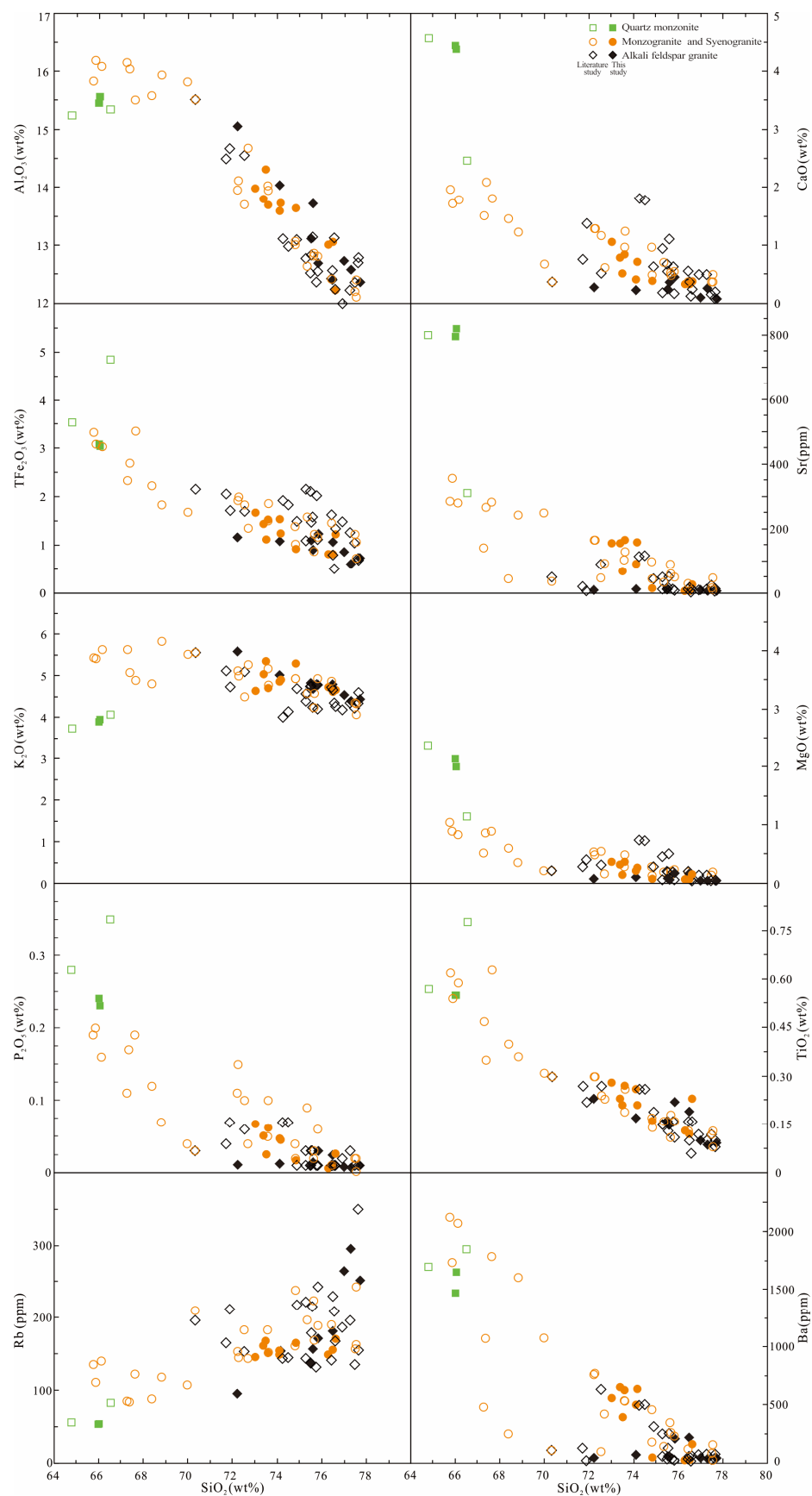


**Figure 12.** Plots of major and trace elements vs. SiO<sub>2</sub> for the Qingdao granitoids. The literature data sources are from [11,15,17].

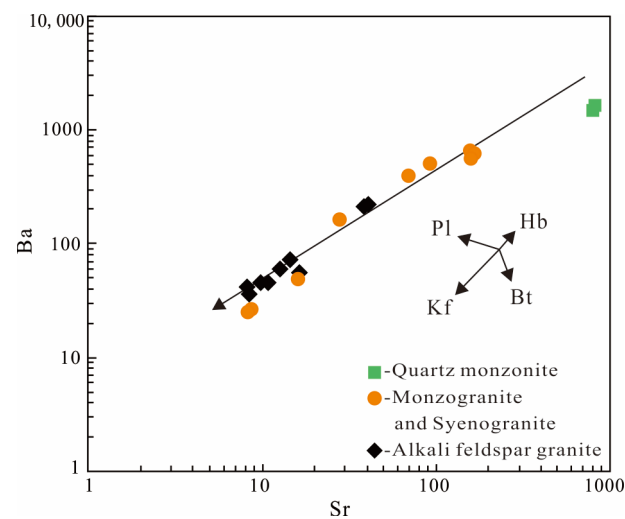


**Figure 13.** Ba vs. Sr plot (modified after [52]). Pl: plagioclase; Kfs: K-feldspar; Bt: biotite; Hbl: hornblende).

The monzogranite and syenogranite have high  $(^{87}\text{Sr}/^{86}\text{Sr})_i$  ratios but negative  $\varepsilon_{\text{Hf}}(t)$  and  $\varepsilon_{\text{Nd}}(t)$  values (Figures 11 and 14, Table S3). Their Sr–Nd isotopic compositions fall into the range of both eclogites and granitic gneisses. These rocks are characterized by high contents of  $\text{SiO}_2$  and  $\text{K}_2\text{O}$ ; low  $\text{Fe}_2\text{O}_3$ ,  $\text{MgO}$ , and  $\text{TiO}_2$  contents; and depletion of Nb, Ta, P, Sr, and Ba, which is like the trace element distribution of the Sulu granitic gneisses [53–55]. In addition, they show low  $\varepsilon_{\text{Hf}}(t)$  values (−13 to −25) and old two-stage model ages (2.7–2.0 Ga) (Figure 14), which show the affinity of the basement of the NCC [56,57]. So, the monzogranite and syenogranite were most likely produced by the partial melting of ancient crustal rocks, represented by granitic gneisses.

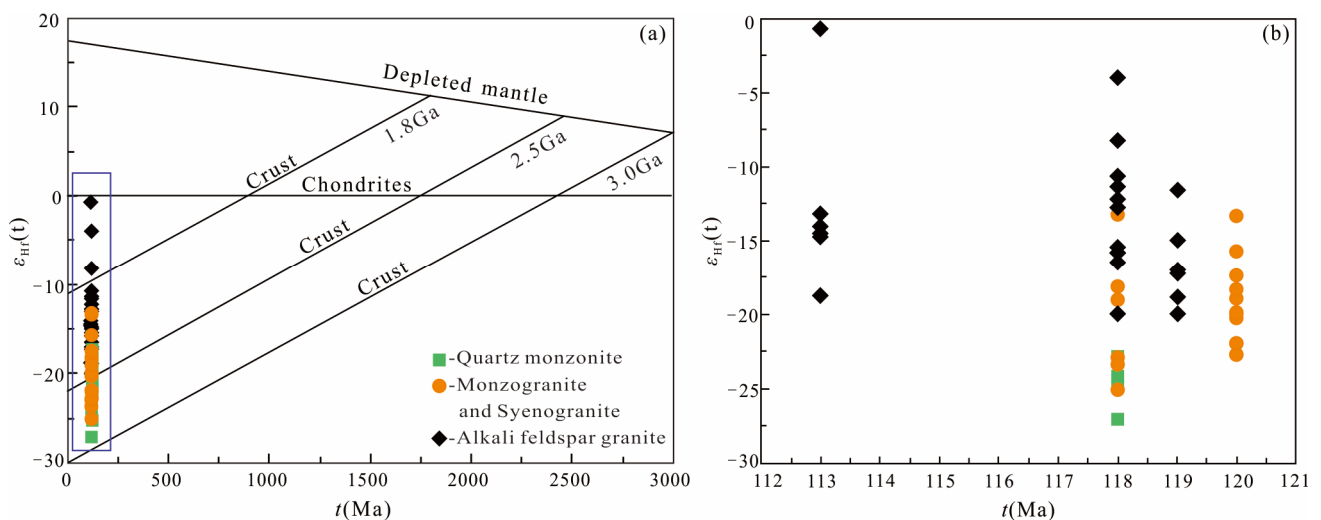


**Figure 14.** Zircon Hf isotope diagrams. (a) Variations of Hf isotopic data with time for depleted mantle and crust. (b) Inset diagram in a showing the zircon Hf isotopic features for granitoids from the Qingdao area.

### 5.2.3. The Alkali Feldspar Granite

The alkali feldspar granites are characterized by high contents of  $\text{SiO}_2$  and total alkalis (Figure 6a), but low contents of  $\text{CaO}$ ,  $\text{MgO}$ , and  $\text{Al}_2\text{O}_3$  (Figure 12). They exhibit significant Eu anomalies and high zircon saturation temperatures, which are typical of A-type granites. As shown in Figure 8, the value of  $(\text{Zr} + \text{Nb} + \text{Ce} + \text{Y})$  ranges from 282 to 455 ppm and the  $10,000 \times \text{Ga}/\text{Al}$  values are between 2.32 and 3.20. Most of these values are higher than

the lower limits of A-type granites. Therefore, the alkali feldspar granites are classified as A-type. Meanwhile, the A-type granites can generally be divided into A<sub>1</sub> and A<sub>2</sub> chemical subclasses based on their Y/Nb ratios [58]. As shown in Figure 15, the alkali feldspar granite samples fall into the A<sub>1</sub>-type field according to the characteristics of trace elements. The A<sub>1</sub>-type granites commonly derived from fractional crystallization of mantle-derived mafic magmas, and also contains peralkaline minerals. However, the A<sub>1</sub>-type granites in the Qingdao region exhibit high SiO<sub>2</sub> but low MgO and negative  $\epsilon_{\text{Hf}}(t)$  values (−10.10 to −17.95), as well as lacking in peralkaline minerals, suggesting that the derivation was mainly from the continental crust rather than mantle-derived magmas.

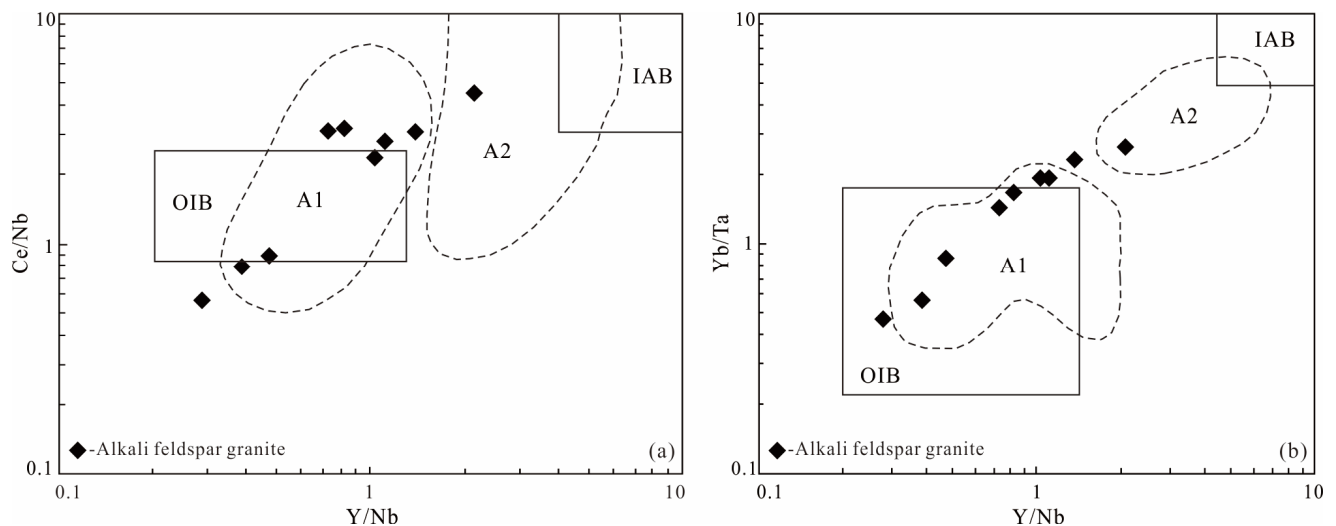


**Figure 15.** (a) Yb/Ta vs. Y/Nb and (b) Y/Nb vs. Ce/Nb diagrams for A-type granite (modified after [57]). OIB = ocean island basalt; IAB = island arc basalt).

The A<sub>1</sub>-type granites in the Qingdao area are characterized by high SiO<sub>2</sub>, K<sub>2</sub>O + Na<sub>2</sub>O contents but low Zr contents and zircon saturation temperature, as well as significantly negative Eu anomalies, which are geochemical features similar to those of aluminous A-type granites. Generally, the aluminous A-type granites are derived from the partial melting of Archean tonalites, trondhjemites, and granodiorites (TTGs) that have high Y/Nb ratios (>1.20) and belong to A<sub>2</sub>-type granites [59]. However, the A<sub>1</sub>-type granites in the Qingdao area have low Y/Nb ratios (0.28~2.14) and low zircons saturation temperature ( $T_{\text{Zr}} = 784\text{--}837\text{ }^{\circ}\text{C}$ ). They are unlikely to have been derived from the partial melting of TTGs.

As shown in Figure 12, non-adakitic granites and A-type granites show a similar crystallization trend and similar saturation temperatures of zircon (the former slightly higher than the latter), suggesting that the A-type granites may be formed through fractional crystallization from the non-adakitic granitic magma in the Qingdao area. There was a significant correlation between the Rb/Sr, Rb/V ratio, and Rb contents in Figure 16, which proves that crystallization plays a dominant role in the magmatic evolution and confirms the evolution relationship between non-adakitic granites and A-type granites in the Qingdao area. The low Y/Nb ratios are controlled by the fractional crystallization of amphibole and plagioclase. As shown in Figure 13, alkali feldspar is a fractionation phase, which can also interpret the Ba and Sr depletion, while the strong negative Eu anomalies are considered to be connected with plagioclase fractionation. The characteristics of P and Ti are attributed to the fractionation of apatite and ilmenite.

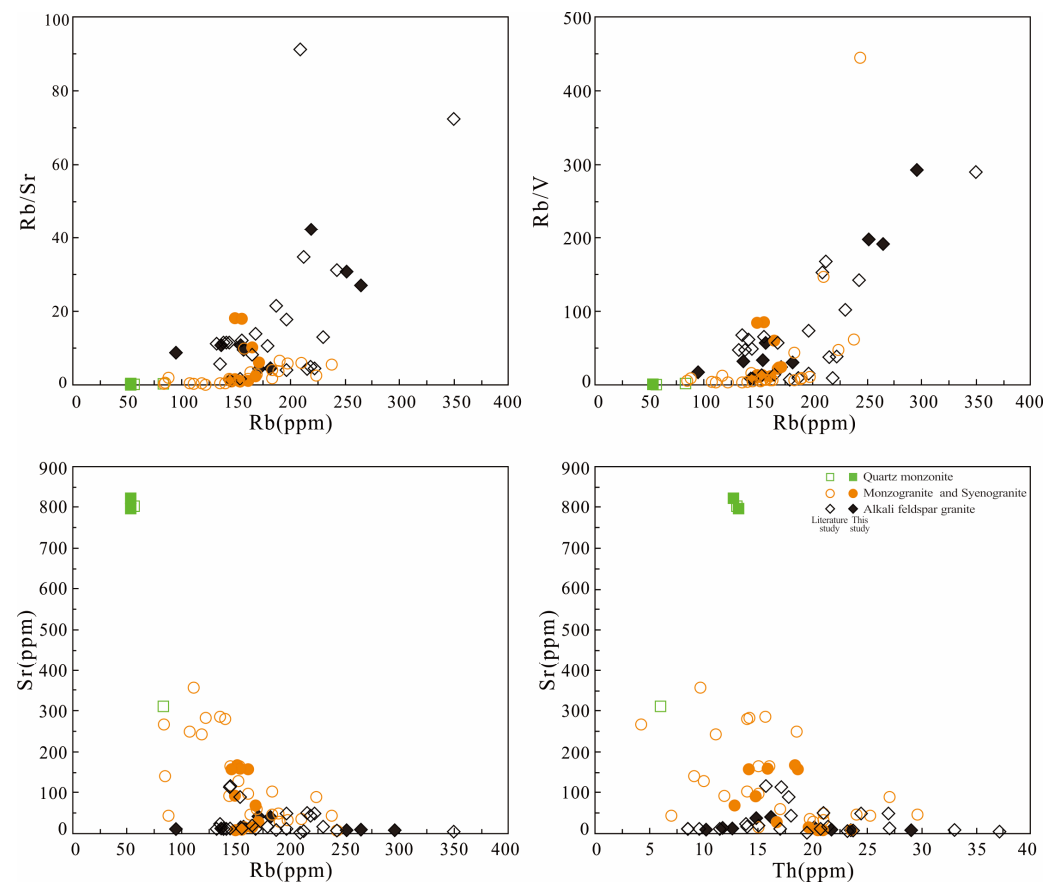


**Figure 16.** Correlograms for trace elements ratios of the Qingdao granitoids. The literature data sources are from [11,15,17].

### 5.3. Tectonic Significance and Granite Magmatism

The studied granitoids in the Qingdao area originated from the dehydration melting of the thickened crust and the zircon saturation temperature of the granitoids can reach 675 °C–810 °C. The saturation temperature indicates the upper limit of the magma temperature for inheritance-rich granites (>10% residual zircons) but is only an estimate of magma temperature for inheritance-poor granitoids [60]. The Qingdao granitoids contain almost no residual zircons based on the U–Pb ages and CL images (Figures 3 and 4). Therefore, the saturation temperature of these granitoids represents the magmatic temperature. It is difficult to get such high melting temperatures without heat supply from the mantle [61]. Therefore, the dehydration and melting of crustal materials in the study area may be related to mantle-derived magma underplating. According to the geochemical characteristics of the adakite-like granitoids, the magma formation depths are more than 50 km, which is thicker than the current average depth of the crust (35 km) [62–66], indicating that there was still a thick crust in some regions of the eastern NCC and Sulu belt at ~120 Ma. Zircon U–Pb dating shows that both normal granitoids and adakite-like granitoids intruded the eastern NCC about 120 Ma ago. There was a lack of adakitic rocks but widespread distribution of normal granites after 120 Ma, suggesting further that the lithosphere beneath the eastern North China Craton was removed at ~120 Ma beneath the Jiaodong Peninsula.

There were various tectonic causes that lead to lithospheric thinning in the NCC, including (1) the collision of the NCC and SCB [63,64], (2) a mantle superplume [67–69], and (3) the subduction of the Paleo-Pacific plate [45,70–72]. Some scholars believed that the collision of the NCC and SCB in the Triassic resulted in the thickening of the crust and the formation of a large volume of eclogites, which caused the delamination of the lithosphere. However, it is difficult to explain why the thickening of the crust in the Triassic did not cause delamination until 100 Ma [73]. Furthermore, the collision occurred in the

west of the NCC, but the thinning mainly occurred in the east. Moreover, the orogenic belts formed by the collision of the NCC and SCB were distributed in the E–W direction, while the lithospheric thinning areas were distributed in the N–NE direction, which is not consistent with the distribution direction of the orogenic belts. Therefore, the collision of the NCC and SCB was only the tectonic basis of lithospheric thinning rather than the triggering factor [74]. Other scholars believed that the mantle upwelling affected the evolution of eastern China and led to the destruction of the NCC. However, there is still a lack of evidence for the existence of mantle superplume beneath the NCC during the Mesozoic. The eastern China continent shows a trend of being thick in the west and thin in the east at present, which is consistent with the subduction direction of the Paleo-Pacific plate in the Mesozoic. Geophysical data show that a high velocity anomaly appears in the eastern China continent within the depth range 930–1120 km, which may be related to the subduction of the Paleo-Pacific plate [75,76]. The subduction of the Paleo-Pacific plate was the most likely trigger for a lithospheric extensional environment in the eastern China during the Cretaceous due to the rollback process of the Paleo-Pacific slab [73,76,77]. It has been proposed that subduction of the Paleo-Pacific plate beneath the Eurasian plate was initiated at ca. 180–170 Ma [78,79]. The subduction angle changed from shallow to deep during the Late Jurassic, and slab rollback of which the rate reached the maximum in the Early Cretaceous at ca. 130–120 Ma [80]. Once the Paleo-Pacific plate is decoupled from the mantle wedge, the slab–mantle interface is heated by lateral incursion of the asthenospheric mantle to allow the dehydration melting of rocks in the metasomatized mantle wedge base. The partial melting of the mantle resulted in magma underplating, which provided the heat source. The continuous underplating caused the almost simultaneous partial melting of lower and middle crusts to form quartz monzonite and granite, respectively. The density of UHP eclogite partial melting residue is much higher than that of normal eclogite. The gravity of the high-density residue tended to be unstable, which was more conducive to the delamination and uplift of the orogenic belt, resulting in a large-scale crustal thinning in the eastern NCC and Sulu belt during the Early Cretaceous (Figure 17).

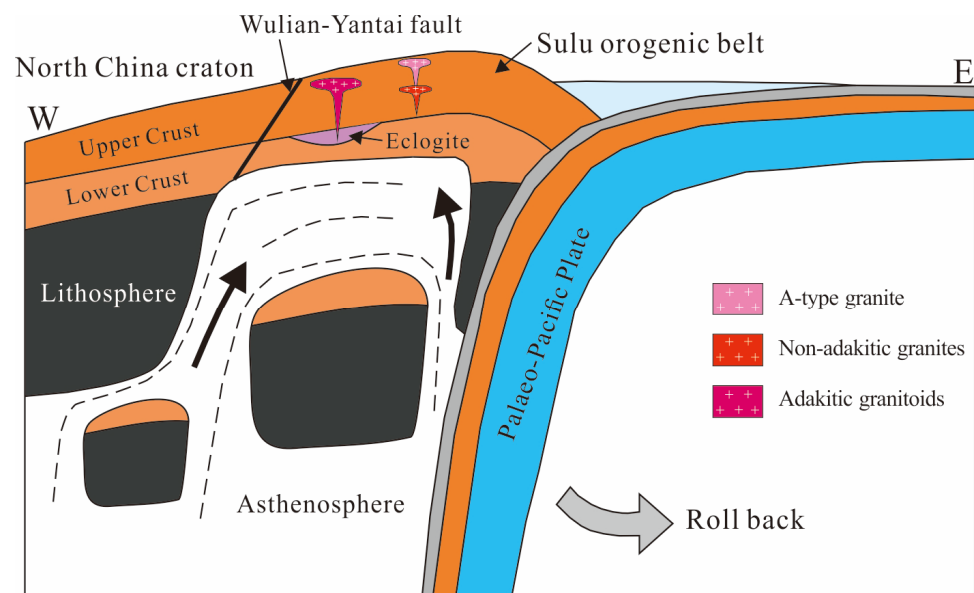


**Figure 17.** Tectonic model for the generation and emplacement of the Qingdao granitoids.

## 6. Conclusions

- (1) The granitoids in the Qingdao area include quartz monzonite, monzogranite, syenogranite, and alkali feldspar granite, which were all emplaced during the Early Cretaceous (120.5–113.1 Ma).

- (2) Quartz monzonite, characterized by adakitic features, may have been produced by the partial melting of phengite-bearing eclogites at the base of the thickened crust with crustal material from the NCC.
- (3) The monzogranite and syenogranite belong to highly fractionated I-type granites, and may be derived from the continental material of the NCC. The I-type monzogranite and syenogranite were most likely produced through the partial melting of granitic gneisses from the NCC. The A-type alkali feldspar granite may be formed through fractional crystallization from the non-adakitic granitic magma.
- (4) The Qingdao granitoids were likely formed under a lithospheric extensional environment due to the rollback process of the Paleo-Pacific slab, which in turn resulted in the partial melting of the residual UHP eclogite and granitic gneisses in the Sulu orogenic belt.

**Supplementary Materials:** The following supporting information can be downloaded at: <https://www.mdpi.com/article/10.3390/min13070963/s1>, Table S1: LA-ICP-MS zircon U-Pb data of the Qingdao granitoids; Table S2: Zircon Hf isotopic data of the Qingdao granitoids; Table S3: Whole-rock major and trace elements and Sr-Nd isotopes of the Qingdao granitoids.

**Author Contributions:** Conceptualization, Y.D. and X.B.; methodology, H.Z.; formal analysis, S.Z.; investigation, M.L.; data curation, X.B.; writing—original draft preparation, Y.D. and X.B.; writing—review and editing, Y.D., X.B. and H.Z. All authors have read and agreed to the published version of the manuscript.

**Funding:** This work was financially supported by National Natural Science Foundation of China (41802211; 42203066) and the Natural Science Foundation of Shandong Province (ZR2020QD027).

**Data Availability Statement:** The data presented in this study are available in the Supplementary Materials.

**Acknowledgments:** The authors are grateful to reviewers and editors for their constructive comments that improved this manuscript.

**Conflicts of Interest:** The authors declare no conflict of interest.

## References

1. Zhai, M.G.; Cong, B.L.; Guo, J.H.; Liu, W.J.; Li, Y.G.; Wang, Q.C. Sm–Nd geochronology and petrography of garnet pyroxene granulites in the northern Sulu region of China and their geotectonic implication. *Lithos* **2000**, *52*, 23–33. [[CrossRef](#)]
2. Wu, Y.B.; Zheng, Y.F. Tectonic evolution of a composite collision orogen: An overview on the Qinling–Tongbai–Hong’an–Dabie–Sulu orogenic belt in central China. *Gondwana Res.* **2013**, *23*, 1402–1428.
3. Li, S.Z.; Jahn, B.M.; Zhao, S.J.; Dai, L.M.; Li, X.Y.; Suo, Y.H.; Guo, L.L.; Wang, Y.M.; Liu, X.C.; Lan, H.Y.; et al. Triassic southeastward subduction of North China Block to South China Block: Insights from new geological, geophysical and geochemical data. *Earth-Sci. Rev.* **2017**, *166*, 270–285. [[CrossRef](#)]
4. Yang, W.C. Geophysical profiling across the Sulu ultra-high-pressure metamorphic belt, eastern China. *Tectonophysics* **2002**, *3–4*, 277–288. [[CrossRef](#)]
5. Chen, M.; Zheng, J.; Sun, M.; Zhao, J. Mid-Neoproterozoic crustal evolution of the northeastern Yangtze Block: Evidence from the felsic-gneiss xenoliths hosted in the Donghai Cenozoic basalts. *J. Asian Earth Sci.* **2013**, *66*, 108–122. [[CrossRef](#)]
6. Zheng, J.P.; Tang, H.Y.; Xiong, Q.; Griffin, W.L.; O’Reilly, S.Y.; Pearson, N.; Zhao, J.H.; Wu, Y.B.; Zhang, J.F.; Liu, Y.S. Linking continental deep subduction with destruction of a cratonic margin: Strongly reworked North China SCLM intruded in the Triassic Sulu UHP belt. *Contrib. Mineral. Petrol.* **2014**, *168*, 1028. [[CrossRef](#)]
7. Zhao, R.; Wang, Q.; Liu, X.; Wang, W.; Pan, R. Architecture of the Sulu crustal suture between the North China Craton and Yangtze Craton: Constraints from Mesozoic granitoids. *Lithos* **2016**, *266–267*, 348–361. [[CrossRef](#)]
8. Yang, J.H.; Wu, F.Y.; Chung, S.L.; Wilde, S.A.; Chu, M.F.; Lo, C.H.; Song, B. Petrogenesis of Early Cretaceous intrusions in the Sulu ultrahigh-pressure orogenic belt, east China and their relationship to lithospheric thinning. *Chem. Geol.* **2005**, *222*, 200–231. [[CrossRef](#)]
9. Zhao, Z.F.; Liu, Z.; Chen, Q. Melting of subducted continental crust: Geochemical evidence from Mesozoic granitoids in the Dabie-Sulu orogenic belt, east-central China. *J. Asian Earth Sci.* **2017**, *145*, 260–277.
10. Wang, S.J.; Schertl, H.; Pang, Y.M. Geochemistry, geochronology and Sr–Nd–Hf isotopes of two types of early Cretaceous granitic porphyry dykes in the Sulu orogenic belt, eastern China. *Can. J. Earth Sci.* **2019**, *57*, 249–266. [[CrossRef](#)]
11. Zhao, G.T.; Wang, D.Z.; Cao, Q.C. THE Geochemistry and genesis of the Laoshan granitoids, Shandong Province. *Geol. J. China Univ.* **1997**, *3*, 1–15. (In Chinese with English abstract)

12. Huang, F.; Li, S.G.; Dong, F.; Li, Q.L.; Wang, Y.; Yang, W. Recycling of deeply subducted continental crust in the Dabie Mountains, central China. *Lithos* **2007**, *96*, 151–169. [[CrossRef](#)]
13. Liu, S.; Hu, R.; Gao, S.; Feng, C.X.; Qi, Y.Q.; Wang, T.; Feng, G.Y.; Coulson, I.M. U-Pb zircon age, geochemical and Sr-Nd-Pb-Hf isotopic constraints on age and origin of alkaline intrusions and associated mafic dikes from Sulu orogenic belt, Eastern China. *Lithos* **2008**, *106*, 365–379. [[CrossRef](#)]
14. Wang, R.C.; Wang, D.Z.; Zhao, G.T.; Lu, J.J.; Chen, X.M.; Xu, S.J. Accessory Mineral Record of Magma-Fluid Interaction in the Laoshan I- and A-Type Granitic Complex, Eastern China. *Phys. Chem. Earth Part A* **2001**, *26*, 835–849. [[CrossRef](#)]
15. Yan, Q.S.; Shi, X.F. Geochemistry and petrogenesis of the Cretaceous A-type granites in the Laoshan granitic complex, eastern China. *Isl. Arc* **2014**, *23*, 221–235. [[CrossRef](#)]
16. Wang, H.; Wang, S.; Xu, Z.; Fu, B.; Zhao, Z.; Li, Z.; Dong, Y.; Tang, L.; Li, J. Geochemical and Sr-Nd-Pb-Hf-O isotopic compositions of the Tiezhai complex: Implications for lithosphere destruction of the North China Craton. *Gondwana Res.* **2018**, *61*, 203–221. [[CrossRef](#)]
17. Gao, Y.J.; Niu, Y.L.; Duan, M.; Xue, Q.Q.; Sun, P.; Chen, S.; Xiao, Y.Y.; Guo, P.Y.; Wang, X.H.; Chen, Y.H. The petrogenesis and tectonic significance of the Early Cretaceous intraplate granites in eastern China: The Laoshan granite as an example. *Lithos* **2019**, *328–329*, 200–210. [[CrossRef](#)]
18. Li, S.Z.; Kusky, T.M.; Zhao, G.C.; Liu, X.C.; Wang, L.; Kopp, H.; Hoernle, K.; Zhang, G.W.; Dai, L.M. Thermochronological constraints on two-stage extrusion of HP/UHP terranes in the Dabie-Sulu orogen, east-central China. *Tectonophysics* **2011**, *504*, 25–42. [[CrossRef](#)]
19. Vermeesch, P. IsoplotR: A free and open toolbox for geochronology. *Geosci. Front.* **2018**, *9*, 15. [[CrossRef](#)]
20. Rollinson, H. *Using Geochemical Data: Evaluation, Presentation, Interpretation*; Longman Scientific and Technical: New York, NY, USA, 1993; pp. 1–352.
21. Middlemost, E.A.K. Naming materials in the magma/igneous rock system. *Earth-Sci. Rev.* **1994**, *37*, 215–224. [[CrossRef](#)]
22. Streckeisen, A.; Le Maitre, R. A chemical approximation to the modal QAPF classification of the igneous rocks. *Neues Jahrb. Für Mineral. Abh.* **1979**, *136*, 169–206.
23. Boehnke, P.; Watson, E.B.; Trail, D.; Harrison, T.M.; Schmitt, A.K. Zircon saturation revisited. *Chem. Geol.* **2013**, *351*, 324–334. [[CrossRef](#)]
24. Sun, S.S.; McDonough, W.F. Chemical and isotopic systematics of oceanic basalts: Implications for mantle composition and processes. *Geol. Soc.* **1989**, *42*, 313–345. [[CrossRef](#)]
25. Guo, J.H.; Chen, F.K.; Zhang, X.M.; Siebei, W.; Zhai, M.G. Evolution of syn- to post-collisional magmatism from North Sulu UHP belt, eastern China: Zircon U-Pb geochronology. *Acta Petrol. Sin.* **2005**, *21*, 1281–1301. (In Chinese with English abstract)
26. Qiu, H.B.; Lin, W.; Chen, Y.; Michel, F. Jurassic–Early Cretaceous tectonic evolution of the North China Craton and Yanshanian intracontinental orogeny in East Asia: New insights from a general review of stratigraphy, structures, and magmatism. *Earth-Sci. Rev.* **2023**, *237*, 104320. [[CrossRef](#)]
27. Liu, J.B.; Ye, K.; Maruyama, S.; Cong, B.; Fan, H.R. Mineral inclusions in zircon from gneiss in the ultra-high pressure zone of the Dabie Mountains, China. *J. Geol.* **2001**, *109*, 523–535. [[CrossRef](#)]
28. Zheng, Y.F.; Chen, R.X.; Zhao, Z.F. Chemical geodynamics of continental subduction-zone metamorphism: Insights from studies of the Chinese Continental Scientific Drilling (CCSD) core samples. *Tectonophysics* **2009**, *475*, 327–358. [[CrossRef](#)]
29. Zhao, Z.F.; Zheng, Y.F.; Wei, C.S.; Wu, Y.B. Post-collisional granitoids from the Dabie orogen in China: Zircon U-Pb age, element and O isotope evidence for recycling of subducted continental crust. *Lithos* **2007**, *93*, 248–272. [[CrossRef](#)]
30. Zhang, J.; Zhao, Z.F.; Zheng, Y.F.; Dai, M.N. Postcollisional magmatism: Geochemical constraints on the petrogenesis of Mesozoic granitoids in the Sulu orogen, China. *Lithos* **2010**, *119*, 512–536. [[CrossRef](#)]
31. Whalen, J.B.; Currie, K.L.; Chappell, B.W. A-type granites: Geochemical characteristics, discrimination and petrogenesis. *Contrib. Mineral. Petrol.* **1987**, *95*, 407–419. [[CrossRef](#)]
32. Defant, M.J.; Drummond, M.S. Mount St. Helens: Potential example of the partial melting of the subducted lithosphere in a volcanic arc. *Geology* **1993**, *21*, 547–550. [[CrossRef](#)]
33. Castillo, P.R.; Janney, P.E.; Solidum, R.U. Petrology and geochemistry of Camiguin Island, southern Philippines: Insights to the source of adakites and other lavas in a complex arc setting. *Contrib. Mineral. Petrol.* **1999**, *134*, 33–51. [[CrossRef](#)]
34. Castillo, P.R. An overview of adakite petrogenesis. *Chin. Sci. Bull.* **2006**, *51*, 257–268. [[CrossRef](#)]
35. Richards, J.P.; Spell, T.; Rameh, E.; Raziq, A.; Fletcher, T. High Sr/Y magmas reflect arc maturity, high magmatic water content, and porphyry Cu ± Mo ± Au potential: Examples from the Tethyan arcs of Central and Eastern Iran and Western Pakistan. *Econ. Geol.* **2012**, *107*, 295–332. [[CrossRef](#)]
36. Zhong, S.; Seltnann, R.; Shen, P. Two different types of granitoids in the Suyunhe large porphyry Mo deposit, NW China and their genetic relationships with molybdenum mineralization. *Ore Geol. Rev.* **2017**, *88*, 116–139. [[CrossRef](#)]
37. Chen, B.; Jahn, B.M.; Wei, C. Petrogenesis of Mesozoic granitoids in the Dabie UHP complex, Central China: Trace element and Nd-Sr isotope evidence. *Lithos* **2002**, *60*, 67–88. [[CrossRef](#)]
38. Kay, R.W.; Mahlburg, K.S. Delamination and delamination magmatism. *Tectonophysics* **1993**, *219*, 177–189. [[CrossRef](#)]
39. Xu, J.F.; Shinjo, R.; Defant, M.J.; Wang, Q.; Rapp, R.P. Origin of Mesozoic adakitic intrusive rocks in the Ningzhen area of east China: Partial melting of delaminated lower continental crust? *Geology* **2002**, *30*, 1111–1114. [[CrossRef](#)]

40. Wang, Q.; Xu, J.F.; Jian, P.; Bao, Z.W.; Zhao, Z.H.; Li, C.F.; Xiong, X.L.; Ma, J.L. Petrogenesis of adakitic porphyries in an extensional tectonic setting, Dexing, South China: Implications for the genesis of porphyry copper mineralization. *J. Petrol.* **2006**, *47*, 119–144. [[CrossRef](#)]
41. Guo, J.; Dai, L.Q.; Zheng, Y.F.; Zhao, Z.F. Mesozoic reworking of the Paleozoic subducted continental crust beneath the south-central margin of the North China Block: Geochemical evidence from granites in the Xiaoqinling-Xiong'er shan region. *Lithos* **2021**, *402–403*, 105886. [[CrossRef](#)]
42. Zhao, Z.F.; Zheng, Y.-F.; Wei, C.-S.; Wu, Y.-B.; Chen, F.K.; Jahn, B.-M. Zircon U-Pb age, element and C-O isotope geochemistry of post-collisional Mafic-ultramafic rocks from the Dabie orogen in east-central China. *Lithos* **2005**, *83*, 1–28. [[CrossRef](#)]
43. Zhao, Z.F.; Zheng, Y.F. Remelting of subducted continental lithosphere: Petrogenesis of Mesozoic magmatic rocks in the Dabie-Sulu orogenic belt. *Sci. China Ser. D Earth Sci.* **2009**, *52*, 1295–1318. [[CrossRef](#)]
44. Li, X.Y.; Li, S.Z.; Huang, F.; Wang, Y.M.; Yu, S.Y.; Cao, H.H.; Xie, W.M. Petrogenesis of high Ba-Sr plutons with high Sr/Y ratios in an intracontinental setting: Evidence from Early Cretaceous Fushan monzonites, central North China Craton. *Geol. Mag.* **2019**, *156*, 1965–1981. [[CrossRef](#)]
45. Tang, J.; Zheng, Y.F.; Wu, Y.B.; Gong, B.; Liu, X. Geochronology and geochemistry of metamorphic rocks in the jiaobei terrane: Constraints on its tectonic affinity in the sulu orogen. *Precambrian Res.* **2007**, *152*, 48–82. [[CrossRef](#)]
46. Zhang, X.R.; Zhao, G.C.; Eizenhöfer, P.R.; Sun, M.; Han, Y.G.; Hou, W.Z.; Liu, D.X.; Wang, B.; Liu, Q.; Xu, B. Late Ordovician adakitic rocks in the Central Tianshan block, NW China: Partial melting of lower continental arc crust during back-arc basin opening. *Geol. Soc. Am. Bull.* **2016**, *128*, 1367–1382. [[CrossRef](#)]
47. Drummond, M.S.; Defant, M.J. A model for trondhjemite-tonalite-dacite genesis and crustal slab melting: Archean to modern comparisons. *J. Geophys. Res.* **1990**, *95*, 21503–21521. [[CrossRef](#)]
48. Rapp, R.P.; Watson, E.B.; Miller, C.F. Partial melting of amphibolite/eclogite and the origin of Archean trondhjemites and tonalites. *Precambrian Res.* **1991**, *51*, 1–25. [[CrossRef](#)]
49. Peacock, S.M.; Rushme, T.; Thompson, A.B. Partial melting of subducting oceanic crust. *Earth Planet. Sci. Lett.* **1994**, *121*, 227–244. [[CrossRef](#)]
50. Liu, Q.; Jin, Z.M.; Zhang, J.F. An experimental study of dehydration partial melting of a phengite-bearing eclogite at 1.5–3.0 GPa. *Chin. Sci. Bull.* **2009**, *54*, 2090–2100.
51. Liu, S.; Hu, R.; Gao, S.; Feng, C.; Yu, B.; Qi, Y. Zircon U-Pb age, geochemistry and Sr-Nd-Pb isotopic compositions of adakitic volcanic rocks from jiaodong, shandong province, eastern china: Constraints on petrogenesis and implications. *J. Asian Earth Sci.* **2009**, *35*, 445–458. [[CrossRef](#)]
52. Janoušek, V.; Finger, F.; Roberts, M.; Frýda, J.; Pin, C.; Dolejš, D. Deciphering the petrogenesis of deeply buried granites: Whole-rock geochemical constraints on the origin of largely undepleted felsic granulites from the Moldanubian Zone of the Bohemian Massif. *Trans. R. Soc. Edinb. Earth Sci.* **2004**, *95*, 141–159. [[CrossRef](#)]
53. Xu, H.J.; Ye, K.; Song, Y.R.; Chen, Y.; Zhang, J.F.; Liu, Q.; Guo, S. Prograde metamorphism, decompressional partial melting and subsequent melt fractional crystallization in the Weihai migmatitic gneisses, Sulu UHP terrane, eastern China. *Chem. Geol.* **2013**, *341*, 16–37. [[CrossRef](#)]
54. Xue, H.M.; Liu, F.L.; Meng, F.C. Major and trace element geochemistry of granitic gneisses from Sulu orogen, eastern Shandong Peninsula; evidence for a Neoproterozoic active continental margin in the northern margin of the Yangtze craton. *Acta Petrol. Sin.* **2006**, *22*, 1779–1790, (In Chinese with English abstract).
55. Li, X.H.; Chen, F.K.; Li, C.F.; Zhang, H.F.; Guo, J.H.; Yang, Y.H. Zircon ages and Hf isotopic composition gneisses from the Rongcheng ultrahigh-pressure terrain in the Sulu orogenic belt. *Acta Petrol. Sin.* **2007**, *23*, 351–368, (In Chinese with English abstract).
56. Zhao, G.C.; Zhai, M.G. Lithotectonic elements of Precambrian basement in the North China Craton: Review and tectonic implications. *Gondwana Res.* **2013**, *23*, 1207–1240. [[CrossRef](#)]
57. Li, S.S.R. Crustal evolution in the central part of eastern ncc: Zircon u-pb ages from multiple magmatic pulses in the luxi area and implications for gold mineralization. *Ore Geol. Rev.* **2014**, *60*, 126–145.
58. Eby, G.N. Chemical subdivision of the A-type granitoids petrogenetic and tectonic implications. *Geology* **1992**, *20*, 641–644. [[CrossRef](#)]
59. King, P.L.; White, A.; Chappell, B.W.; Allen, C.M. Characterization and Origin of Aluminous A-type Granites from the Lachlan Fold Belt, Southeast Australia. *J. Petrol.* **1997**, *38*, 371–379. [[CrossRef](#)]
60. Miller, C.F.; McDowell, S.M.; Mapes, R.W. Hot and cold granites? Implications of zircon saturation temperatures and preservation of inheritance. *Geology* **2003**, *31*, 529–532. [[CrossRef](#)]
61. Patiño-Douce, A.E.; Beard, J.S. Dehydration-melting of biotite gneiss and quartz amphibolite from 3 to 15 kbar. *J. Petrol.* **1995**, *36*, 707–738. [[CrossRef](#)]
62. Menzies, M.A.; Fan, W.; Zhang, M. Palaeozoic and Cenozoic lithoprobes and the loss of >120 km of Archaean lithosphere, Sino-Korean Craton, China. *Geol. Soc. Lond. Spec. Publ.* **1993**, *76*, 71–81. [[CrossRef](#)]
63. Menzies, M.A.; Xu, Y.G. Geodynamics of the North China Craton. In *Mantle Dynamics and Plate Interactions in East Asia*; Flower, M.F.J., Chung, S.L., Lo, C.H., Lee, T.Y., Eds.; American Geophysical Union: Washington, DC, USA, 1998; Volume 27, pp. 155–165.
64. Gao, S.; Rudnick, R.L.; Carlson, R.W.; McDonough, W.F.; Liu, Y.S. Re-Os evidence for replacement of ancient mantle lithosphere beneath the North China Craton. *Earth Planet. Sci. Lett.* **2002**, *198*, 307–322. [[CrossRef](#)]

65. Ma, L.; Jiang, S.Y.; Hou, M.L.; Dai, B.Z.; Jiang, Y.H.; Yang, T.; Zhao, K.D.; Pu, W.; Zhu, Z.Y.; Xu, B. Geochemistry of Early Cretaceous talc-alkaline lamprophyres in the Jiaodong Peninsula: Implication for lithospheric evolution of the eastern North China Craton. *Gondwana Res.* **2014**, *25*, 859–872. [[CrossRef](#)]
66. Ma, L.; Jiang, S.Y.; Hofmann, A.W.; Xu, Y.G.; Dai, B.Z.; Hou, M.L. Rapid lithospheric thinning of the North China Craton: New evidence from cretaceous mafic dikes in the Jiaodong Peninsula. *Chem. Geol.* **2016**, *432*, 1–15. [[CrossRef](#)]
67. Wilde, S.A.; Zhou, X.H.; Nemchin, A.A.; Sun, M. Mesozoic crust mantle interaction beneath the North China craton: A consequence of the dispersal of Gondwanaland and accretion of Asia. *Geology* **2003**, *31*, 17–20. [[CrossRef](#)]
68. Deng, J.F.; Mo, X.X.; Zhao, Z.D.; Wu, Z.X.; Luo, Z.H.; Su, S.G. A new model for the dynamic evolution of Chinese lithosphere: ‘continental roots-plume tectonics’. *Earth Sci. Rev.* **2004**, *65*, 223–275. [[CrossRef](#)]
69. Zhao, Z.F.; Zheng, Y.F.; Wei, C.S.; Wu, Y.B. Zircon isotope evidence for recycling of subducted continental crust in post-collisional granitoids from the Dabie terrane in China. *Geophy Res. Lett.* **2004**, *31*, L22602. [[CrossRef](#)]
70. Wu, F.Y.; Lin, J.Q.; Wilde, S.A.; Zhang, X.O.; Yang, J.H. Nature and significance of the Early Cretaceous giant igneous event in eastern China. *Earth Planet. Sci. Lett.* **2005**, *233*, 103–119. [[CrossRef](#)]
71. Sun, W.D.; Ding, X.; Hu, Y.H.; Li, X.H. The golden transformation of the Cretaceous plate subduction in the west Pacific. *Earth Planet. Sci. Lett.* **2007**, *262*, 533–542. [[CrossRef](#)]
72. Xu, Y.G.; Blusztajn, J.; Ma, J.L.; Suzuki, K.; Liu, J.F.; Hart, S.R. Late Archean to Early Proterozoic lithospheric mantle beneath the western North China craton: Sr-Nd-Os isotopes of peridotite xenoliths from Yangyuan and Fansi. *Lithos* **2008**, *102*, 25–43. [[CrossRef](#)]
73. Wu, F.Y.; Xu, Y.G.; Gao, S.; Zheng, J.P. Lithospheric thinning and destruction of the North China Craton. *Petrol. Sin.* **2008**, *24*, 1145–1174. (In Chinese with English abstract)
74. Zheng, J.P.; Griffin, W.L.; O’Reilly, S.Y.; Yu, C.M.; Zhang, H.F.; Pearson, N.; Zhang, M. Mechanism and timing of lithospheric modification and replacement beneath the eastern North China Craton: peridotitic xenoliths from the 100 Ma Fuxin basalts and a regional synthesis. *Geochim. Cosmochim. Acta* **2007**, *71*, 5203–5325. [[CrossRef](#)]
75. Li, J.; Yuen, D.A. Mid-mantle heterogeneities associated with Izanagi plate: Implications for regional mantle viscosity. *Earth Planet. Sci. Lett.* **2014**, *385*, 137–144. [[CrossRef](#)]
76. Li, X.Y.; Li, S.Z.; Suo, Y.H.; Somerville, I.D.; Huang, F.; Liu, X.; Wang, P.C.; Han, Z.X.; Jin, L.J. Early Cretaceous diabbases, lamprophyres and andesites-dacites in western Shandong, North China Craton: Implications for local delamination and Paleo-Pacific slab rollback. *J. Asian Earth Sci.* **2018**, *160*, 426–444.
77. Wang, S.; Wang, L.; Ding, Y.; Wang, Z. Origin and Tectonic Implications of Post-Orogenic Lamprophyres in the Sulu Belt of China. *J. Earth Sci.* **2020**, *31*, 1200–1215. [[CrossRef](#)]
78. Engebretson, D.C.; Cox, A.; Gordon, R.G. Relative motion between oceanic and continental plates in the Pacific basin. *Geol. Soc. Am. Spec. Pap.* **1985**, *206*, 1–55.
79. Wu, F.Y.; Yang, J.H.; Lo, C.H.; Wilde, S.A.; Sun, D.Y.; Jahn, B.M. The Heilongjiang Group: A Jurassic accretionary complex in the Jiamusi Massif at the western Pacific margin of northeastern China. *Isl. Arc* **2007**, *16*, 156–172. [[CrossRef](#)]
80. Zhu, R.X.; Xu, Y.G. The subduction of the west Pacific plate and the destruction of the North China Craton. *Sci. China Earth Sci.* **2019**, *62*, 1340–1350. [[CrossRef](#)]

**Disclaimer/Publisher’s Note:** The statements, opinions and data contained in all publications are solely those of the individual author(s) and contributor(s) and not of MDPI and/or the editor(s). MDPI and/or the editor(s) disclaim responsibility for any injury to people or property resulting from any ideas, methods, instructions or products referred to in the content.